# Sources of Phase Changes in BOLD and CBV-Weighted fMRI

Fuqiang Zhao,[1,2*] Tao Jin,[1] Ping Wang,[1] Xiaoping Hu,[2*] and Seong-Gi Kim[1]

**Phase changes in blood oxygenation-level dependent (BOLD) fMRI have been observed in humans; however, their exact origin has not yet been fully elucidated. To investigate this issue, we acquired gradient-echo (GE) BOLD and cerebral blood volume (CBV)-weighted fMRI data in anesthetized cats during visual stimulation at 4.7T and 9.4T, before and after injection of a superparamagnetic contrast agent (monocrystalline iron oxide nanoparticles, MION), respectively. In BOLD fMRI, large positive changes in both magnitude and phase were observed predominantly in the cortical surface area, where the large draining veins reside. In CBV-weighted fMRI, large negative changes in both magnitude and phase were detected mainly in the middle cortical area, where the greatest CBV change takes place. Additionally, the phase change was temporally correlated with the magnitude response and was linearly dependent on the echo time (TE), which cannot be explained by the intravascular (IV) contribution and functional temperature change. Phase changes with the opposite polarity were also observed in the regions around the dominant phase changes. These phase changes can be explained by the application of the "Lorentz sphere" theory in the presence of relevant activation-induced changes in vessels. The volume-averaged magnetization and its demagnetization are the main sources of fMRI signal phase change. Magn Reson Med 57:520–527, 2007. © 2007 Wiley-Liss, Inc.**

**Key words: phase change; fMRI; Lorentz sphere; volume-averaged magnetization; demagnetization**

Functional magnetic resonance imaging (fMRI) based on blood oxygenation level-dependent (BOLD) (1–3) signal has become a routine tool for studying the brain, particularly in human subjects. As an alternative to BOLD, cerebral blood volume (CBV)-weighted fMRI can be performed with the use of superparamagnetic exogenous intravascular (IV) contrast agents, such as monocrystalline iron oxide nanoparticles (MION), in animal models (4–7). The physical source of both the BOLD and the CBV-weighted fMRI signals is the change in field inhomogeneity generated by the magnetic susceptibility effect in blood due to paramagnetic deoxyhemoglobin or exogenous contrast agents (1). During brain activation, changes in deoxyhemoglobin and blood volume modulate the field inhomogeneity inside and outside blood vessels and thus the spins' coherence, which in turn alters the magnitude of the MRI signal.

The susceptibility effects of blood vessels can be approximately modeled as infinite cylinders (8,9). The resonance frequency of a water proton is shifted from the Larmor frequency due to the susceptibility difference between blood and tissue water. For extravascular (EV) water, the magnetic field change ($\Delta B$) is a sum of magnetic field changes induced by all blood vessels that exhibit magnetic perturbations, and can be written as:

$$\Delta B = \sum_{Blood\ vessels} 2\pi \cdot \Delta\chi \cdot B_0 \cdot \left(\frac{R}{r}\right)^2 \sin^2\theta \cdot \cos(2\varphi) \quad [1]$$

where $\Delta\chi$ is the susceptibility difference between IV blood and surrounding tissue, $R$ is the vessel radius, $r$ is the distance between the point of interest and the center of the vessel in the plane through the point of interest and perpendicular to the vessel, $\theta$ is the angle between the main magnetic field $B_0$ and the vessel orientation, and $\varphi$ is the angle between position vector $\boldsymbol{r}$ in this plane and the projection of $\boldsymbol{B_0}$ in the plane. When the frequency shift induced by $\Delta B$ is integrated around vessels (i.e., $\varphi$ ranges from 0° to 360°), the average frequency shift for all the protons in an imaging voxel is essentially zero (8,9). Therefore, a phase change in EV tissue is not expected to occur during brain activation (8,9). However, phase changes (10–12) and frequency shifts of the functional MR signals (13) have been repeatedly reported. Such changes are commonly attributed to the frequency shift of the IV signal (12) or to the tissue water's frequency shift caused by local brain temperature change (13).

To further investigate the sources of stimulation-induced phase changes, we performed BOLD and CBV-weighted fMRI studies in the cat visual cortex at both 4.7T and 9.4T using gradient-echo (GE) echo-planar imaging (EPI). Since the cortical depth-dependent anatomical structure, spatial specificity of the hemodynamic response, and neural activation of this model are well known from previous studies (14–17), we chose a slice perpendicular to the cortical surface to examine the spatial and temporal relations between the magnitude and phase changes of the fMRI signal. Different echo times (TEs) were also used to ascertain the TE dependence of the magnitude and phase changes. If the IV source is dominant, the phase change is not expected to be linearly dependent on TE and should be minimal in CBV data after the injection of contrast agent, due to the short $T_2$ of blood. If the tissue temperature change is dominant, the phase change is expected to be similar in both BOLD and CBV data.

To provide an alternative explanation of the observed phase change, we adapted the "Lorentz sphere" concept to

[1]Department of Neurobiology, University of Pittsburgh, Pittsburgh, Pennsylvania, USA.

[2]Wallace H. Coulter Department of Biomedical Engineering, Georgia Institute of Technology and Emory University, Atlanta, Georgia, USA.

*Correspondence to: Fuqiang Zhao or Xiaoping Hu, Biomedical Imaging Technology Center, 101 Woodruff Circle, Suite 2001, Atlanta, GA 30322. E-mail: fzhao@bme.gatech.edu or xhu@bme.gatech.edu

Grant sponsor: National Institutes of Health; Grant numbers: EB03375; EB03324; EB02013; NS44589; EB002009; Grant sponsor: National Science Foundation; Grant number: BES 0401627; Grant sponsor: Georgia Research Alliance.

Received 14 March 2006; revised 10 October 2006; accepted 8 November 2006.

DOI 10.1002/mrm.21159
Published online in Wiley InterScience (www.interscience.wiley.com).

model the magnetic field distribution in the tissue consisting of EV water and magnetically susceptible IV blood. This concept was originally introduced to estimate the local magnetic field at the nucleus of interest (18–21), and has been applied to calculate the magnetic field distribution in heterogeneous blood (22) or the hyperpolarized $^{129}$Xe frequency shift in blood (23). With the use of the Lorentz sphere, contributions to the frequency shift of the EV water do not cancel, mostly because of the magnetic field contribution from the volume-averaged magnetization in the activated area, and an fMRI phase change should be detected during the brain activation. The experimental results support the prediction given by the volume-averaged magnetization change due to the Lorentz sphere effect (18–21).

## THEORY

A two-component model can be used to analyze the local magnetic field experienced by a proton (1). In this model, the magnetized blood vessels are embedded into surrounding EV tissue. In each voxel the volume-averaged magnetic susceptibility $\chi$ can be calculated from local volume magnetic susceptibilities of the EV tissue $\chi_t$ and the IV blood $\chi_b$ as

$$\chi = f\chi_b + (1 - f)\chi_t \quad [2]$$

where $f$ is the relative blood volume fraction. In an external magnetic field $\boldsymbol{B_0}$, the volume-averaged magnetization for a voxel at position $\boldsymbol{r}$ is given by

$$\mathbf{M}(\mathbf{r}) = \chi(\mathbf{r}) \cdot \frac{\mathbf{B_0}}{\mu_0} \quad [3]$$

where $\mu_0$ is the magnetic permeability of the vacuum.

Consider a volume of activation (VOA) that exhibits the blood susceptibility and/or the blood volume change during activation. A fictitious Lorentz sphere can be drawn around a position $\boldsymbol{r}$ within the VOA (Fig. 1). The size of the sphere is sufficiently large relative to the size of the vessel segments, such that field contributions from vessel segments outside the sphere to the position $\boldsymbol{r}$ within the sphere can be approximately modeled as magnetic dipoles (18,21). It is assumed that $\boldsymbol{M(r)}$ is macroscopically continuous (18). Based on the law of superposition, the magnetic field at $\boldsymbol{r}$, $\boldsymbol{B(r)}$, can be written as the sum of three components: 1) the main magnetic field $\boldsymbol{B_0}$, 2) the field due to the vessels within the sphere $\boldsymbol{B_b(r)}$, and 3) the field induced from the tissues (including vessels) within the VOA but outside the sphere, which includes the field from the magnetization distribution on the sphere surface ($\frac{\mu_0}{3}\mathbf{M}(\mathbf{r})$) and self-demagnetization field ($\mathbf{B}_d(\mathbf{r})$), which is from the remaining volume and the surface of the VOA (18,21,22,24). Thus, $\boldsymbol{B(r)}$ can be written as

$$\mathbf{B}(\mathbf{r}) = \mathbf{B}_0(\mathbf{r}) + \sum_{\text{Blood vessels}} \mathbf{B}_\text{b}(\mathbf{r}) + \frac{\mu_0}{3}\mathbf{M}(\mathbf{r}) + \mathbf{B}_\text{d}(\mathbf{r}) \quad [4]$$

where $\boldsymbol{B_d(r)}$ depends on the geometry and magnetization distribution within the VOA (19).

In our BOLD and CBV experiments, the blood susceptibility is changed by a stimulation-induced decrease in paramagnetic deoxyhemoglobin concentration and the change of the volume of high susceptibility blood due to vessel dilation, respectively. The magnetic field change is

$$\Delta\mathbf{B}(\mathbf{r}) = \Delta\mathbf{B}_\text{d}(\mathbf{r}) + \frac{\mu_0}{3}\Delta\mathbf{M}(\mathbf{r}) + \sum_{\text{Blood vessels}} \Delta\mathbf{B}_\text{b}(\mathbf{r}) \quad [5]$$

where $\Delta\boldsymbol{B_b(r)}$ is the local magnetic field change from the blood vessels, $\Delta\boldsymbol{B_d(r)}$ is the demagnetization field change caused by the susceptibility change on the surface of the VOA and magnetization distribution change within the VOA, and $\Delta\boldsymbol{M(r)}$ is the volume-averaged magnetization change at $\boldsymbol{r}$ given by

$$\begin{aligned}\Delta\mathbf{M}(\mathbf{r}) &= \Delta\chi(\mathbf{r}) \cdot \frac{\mathbf{B}_0}{\mu_0} \\ &= \{f(\mathbf{r}) \cdot \Delta\chi_\text{b}(\mathbf{r}) + \Delta f(\mathbf{r}) \cdot (\chi_b(\mathbf{r}) - \chi_\text{t}(\mathbf{r}))\} \cdot \frac{\mathbf{B}_0}{\mu_0}, \quad [6]\end{aligned}$$

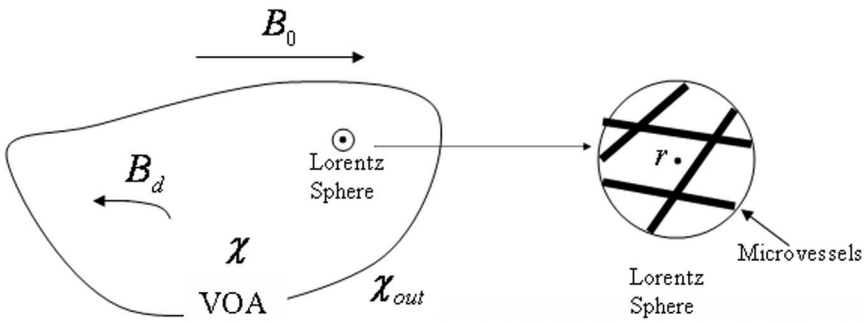


FIG. 1. Diagram for a general magnetic field quantitation of tissue. The VOA with the volume-averaged susceptibility distribution $\chi$ is surrounded by the other tissue with the volume-averaged susceptibility distribution $\chi_{out}$. Main field $\boldsymbol{B_0}$ is applied and the demagnetizing field $\boldsymbol{B_d}$ is induced due to the magnetization of the surrounding tissue inside the VOA. The virtual sphere (Lorentz sphere) is drawn around the site $\boldsymbol{r}$. The enlarged Lorentz sphere is shown on the right side. The blood vessels with high-susceptibility blood are randomly distributed within the sphere. The magnetic field at the site $r$ is the sum of the $\boldsymbol{B_0}$, $\boldsymbol{B_d}$, Lorentz sphere effect and the magnetic field generated by the blood vessels as described by Eq. [4].

where $\Delta\chi_b$ is the blood susceptibility change, and $\Delta f$ is the blood volume change during brain activation. Inserting Eq. [6] into Eq. [5], the phase change at $\boldsymbol{r}$, $\Delta p(\boldsymbol{r})$ can be derived as

$$\Delta p(\mathbf{r}) = -2\pi \cdot \gamma \cdot TE \cdot \left\{ \sum_{Blood\ vessels} \Delta B_b(\mathbf{r}) + \Delta B_d(\mathbf{r}) + \frac{1}{3} \cdot B_0 \cdot [f(\mathbf{r}) \cdot \Delta\chi_b(\mathbf{r}) + \Delta f(\mathbf{r}) \cdot (\chi_b(\mathbf{r}) - \chi_t(\mathbf{r}))] \right\}, \quad [7]$$

Note that from Eq. [7], the phase change is linearly dependent on the TE.

In Eq. [7] the phase change contains three terms. The first term is caused by the field changes from local blood vessels, i.e., the local effect (21,25). The second is the magnetic field change caused by the demagnetization effect, which depends on the geometry and magnitude of susceptibility changes in the VOA. The third arises from the volume-averaged magnetization change. The latter two amount to the bulk magnetic susceptibility (BMS) shift, which originates from distant vessels outside the sphere.

In tissue, the net phase change, which is caused by local fields from all blood vessels within the sphere (i.e., $\sum_{\text{Blood vessels}} \Delta\mathbf{B_b}(\mathbf{r})$), is close to zero because of the randomly distributed microvessels (8,9). However, in the cortical surface, where large draining veins reside, the *net* phase change induced by local vessels is not expected to cancel out completely. If this contribution from the local field is predominant, then positive and negative phase changes can be observed in the cortical surface depending on the vessels' orientation and position.

With this model and a simple anatomical structure of cat visual cortex, a qualitative prediction can be made for the field change (and the phase change). The sign of the phase change depends not only on the volume-averaged magnetization change, but also on the contribution from the demagnetization effect. Roughly, the size of the visual cortex is larger in the posterior–anterior direction, which is roughly parallel to $\boldsymbol{B_0}$, than in the medial–lateral direction in each hemisphere. The field change of an object with its long axis parallel to $\boldsymbol{B_0}$ is dominated by the volume-averaged magnetization change (23). Hence the field change within the visual cortex should be consistent with the corresponding susceptibility change.

In BOLD fMRI, since the venous CBV change (i.e., $\Delta f(\mathbf{r})$) is relatively small, the volume-averaged magnetization decrease is dominated by a venous deoxygenation decrease (i.e., $f(\mathbf{r}) \cdot \Delta\chi_b(\mathbf{r})$). Thus, a positive phase change should be detected in the cortical surface, where the venous blood volume, $f(\mathbf{r})$, is highest (17). In the CBV-weighted fMRI data with the exogenous susceptibility agent, the susceptibility difference between blood and tissue ($\chi_b(\mathbf{r}) - \chi_r(\mathbf{r})$) is large, and the term $\Delta f(\mathbf{r}) \cdot (\chi_b(\mathbf{r}) - \chi_t(\mathbf{r}))$ induced by total CBV change ($\Delta f(\mathbf{r})$) is much larger than $f(\mathbf{r}) \cdot \Delta\chi_b(\mathbf{r})$, the term induced by venous deoxyhemoglobin change. Hence a negative phase change is expected to be dominant in the middle of the cortex, where the greatest CBV increase occurs during activation (17). In the areas surrounding them (the cortical surface for BOLD fMRI and the middle cortex for CBV-weighted fMRI), a reversed change is expected due to the demagnetization effect (which can be intuitively understood as a redistribution of magnetic flux).

## MATERIALS AND METHODS

### Animal Preparation

Eighteen female adolescent cats (0.76–1.56 kg, 10–16 weeks old) were examined in this study. Nine cats were studied at 4.7T (four for the CBV study, one for the consecutive BOLD and CBV studies, and another four for the BOLD study only). A total of nine cats were examined at 9.4T (four for CBV study only, two for the consecutive BOLD and CBV studies, and another three for the BOLD study only) were used with the approval of the Institutional Animal Care and Use Committee of the University of Minnesota. The animals were anesthetized with a ketamine (10–25 mg/kg) and xylazine (2.5 mg/kg) cocktail (i.m.). The animals were orally intubated and mechanically ventilated using a pressure-driven Kent ventilator (~29–30 strokes/min) under isoflurane anesthesia (1–1.3% v/v) in a 70:30 $N_2O$:$O_2$ mixture. The femoral vein and artery were catheterized for fluid supplementation, injection of MION, and blood pressure measurements, respectively. Pancuronium bromide (Elkins-Sinn, Cherry Hill, NJ, USA) mixed in 5% dextrose Ringer's solution was delivered at 0.4 mg/kg/hr via an infusion pump (product no. 55-3333; Harvard Apparatus, MA, USA). During the experiments we continuously recorded arterial blood pressure and end-tidal $CO_2$ (MP150; Biopac Systems Inc., CA, USA). For all studies the mean blood pressure was 80–105 mmHg. We maintained the end-tidal $CO_2$ (Capnomac Ultima; Datex Omeda, Finland) in the range of 3.0–3.8% by adjusting the volume of the respirator (RSP-1002; Kent Scientific, CT, USA). The rectal temperature was maintained at 38.5°C ± 0.5°C with a feedback hot water circulator (models 13-873-206A (Fisher Scientific, Pittsburgh, PA, USA) and U-89000-00 (Cole Parmer, Vernon Hills, IL, USA)). The animals were placed in a cradle and restrained in a postural position by means of a head-holder consisting of ear bars and a bite bar.

For the CBV studies, a bolus of dextran-coated MION (obtained from Ralph Weissleder's laboratory at Massachusetts General Hospital) was injected intravenously with ~1.5 ml/kg 10% dextran solution. A dose of 7.5 mg/kg was used for the 4.7T study, and a dose of 10 mg/kg was used for the 9.4T study (26).

### Experiments and Analyses

MR measurements were performed on either a 9.4T/31 cm (Magnex Scientific, UK) or a 4.7T/40 cm horizontal magnet (Oxford, Oxfordshire, UK). The 9.4T system was equipped with an actively shielded 11-cm-diameter gradient insert, operating at a gradient strength of 18 G/cm and a rise time of 300 μs (Magnex Scientific, Oxford, UK). The 4.7T system was equipped with an in-house-built gradient insert, operating at a gradient strength of 12 G/cm and a rise time of 300 μs. Both MR scanners were driven by identical

Unity INOVA consoles (Varian, Palo Alto, CA, USA). Two 1.6-cm-diameter surface coils provided radiofrequency (RF) transmission and reception at both magnets. Multislice anatomic images were acquired to identify anatomical structures in the brain, and the visual cortex was then positioned in the isocenter of the magnetic field. Magnetic field homogeneity was optimized by manual volume-localized shimming over a $\sim 5 \times 5 \times 5$ mm$^3$ volume of the visual cortex, yielding a water spectral line width of 13–28 Hz.

From multislice GE BOLD scout fMRI and $T_1$-weighted anatomical images, a 2-mm-thick coronal slice orthogonal to the surface of the visual cortex was chosen roughly in the center of the visual cortex (posterior–anterior direction) for fMRI studies. $T_1$-weighted anatomic echo-planar images were obtained with inversion recovery spin-echo EPI to identify the surface of the cortex and the boundary between the gray and white matter. For functional studies, single-shot GE-EPI with an FOV of $2 \times 2$ cm$^2$, a matrix size of $64 \times 64$ (in-plane resolution of $0.3 \times 0.3$ mm$^2$), and a TR of 0.5 s was used. The RF flip angle was adjusted to maximize the signal in the visual cortical area. The GE time was 25 ms for BOLD at 4.7T; 10, 15, 20, and 25 ms for TE-dependent BOLD at 9.4T; 15 and 25 ms for CBV-weighted fMRI at 4.7T; and 10 and 15 ms for CBV-weighted fMRI at 9.4T. Different TE values were interleaved in the same trial. A typical stimulation paradigm was to acquire 60 control, 20 stimulation, and 80 control images. A binocular visual stimulus consisting of moving black and white bar gratings ($\sim$2 cycles/s and 0.2 cycles/degree) (27) was applied, while stationary gratings were presented in the control periods. Approximately 15 GE BOLD and CBV data sets were obtained.

Magnitude and phase images were obtained from the 2D Fourier transformation of the raw *k*-space data. The phase time series was unwrapped on a pixel-by-pixel basis if necessary. The magnitude and phase signals from all fMRI runs under the same conditions were averaged to improve the sensitivity. We obtained functional magnitude and phase maps using the cross-correlation method by comparing time courses with a boxcar function (28). A correlation coefficient (CC) of 0.3 and a minimal cluster size of four pixels were used as thresholds, and yielded the effective $P$-value $< 1 \times 10^{-3}$ (29). The magnitude and phase change maps were calculated for the activated pixels and overlaid on the original echo-planar images. For quantitative analysis, the time courses of active pixels in the phase map were averaged. Based on the averaged time course, the phase and magnitude changes were calculated. Images obtained during the prestimulus control period were taken as the baseline condition because the poststimulus fMRI signal did not return to a prestimulus signal level promptly. Similarly, images acquired within 6 s after the onset of visual stimulation were not used in the quantification of changes due to the slow hemodynamic response.

## RESULTS

### Magnitude and Phase Responses in BOLD fMRI

Figure 2 shows the magnitude (Fig. 2a) and phase-change (Fig. 2b) maps of BOLD fMRI with TE of 25 ms at 4.7T. The highest magnitude increase (yellow pixels in Fig. 2a) was observed near the cortical surface (indicated by the green contours), which is consistent with previous BOLD observations (16,30). In addition, a positive phase change was detected at the cortical surface (red and yellow pixels), where the highest magnitude change was observed. This observation is consistent with previous reports (12,31). In surrounding areas including the scalp (indicated by arrows) and white matter (indicated by black contours), a negative phase change was detected (blue and violet pixels).

To obtain time courses, a region of interest (ROI) based on pixels with significant positive phase changes was selected. Figure 2c illustrates magnitude and phase time courses of the ROI. The temporal evolution of the phase change is similar to that of the magnitude change, suggesting that both changes originate from the identical source, which is the deoxyhemoglobin-induced susceptibility change. The spatial and temporal patterns of both magnitude and phase changes of BOLD at 9.4T (data not shown) are similar to those obtained at 4.7T (Fig. 2).

To further characterize the phase response to neural activity, we collected data with four different TEs (interleaved in the same trial) at 9.4T. The activation maps of both magnitude and phase are similar to those of Fig. 2 (data not shown), irrespective of TE. TE-dependent magnitude and phase changes were obtained from the active ROI (pixels with significant positive phase changes) deter-

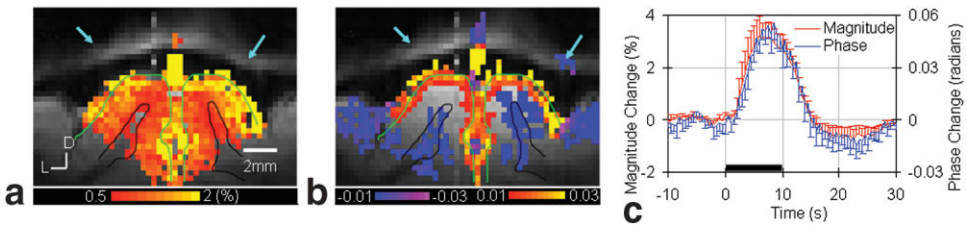


FIG. 2. Phase and magnitude responses in a BOLD study at 4.7T. BOLD magnitude (**a**) and phase-change (**b**) maps of one representative animal are overlaid on the echo-planar images. Green contours delineate the cortical surface, and black contours delineate white matter boundaries. These contours are drawn from the $T_1$-weighted anatomical image. L: lateral, D: dorsal. Cyan arrows point to the scalp. The units of the color bars are the relative signal change for the magnitude, and the radians for the phase. **c:** Averaged phase and magnitude time courses from the positive response pixels of a phase activation map (b) over five animals (mean $\pm$ SEM, $N = 5$). The *y*-axis is the percentage signal change for the magnitude, and the radians for the phase. The black rectangular bar indicates the 10-s stimulus duration. For clarity, only one side of the error bars (SEM) is shown.

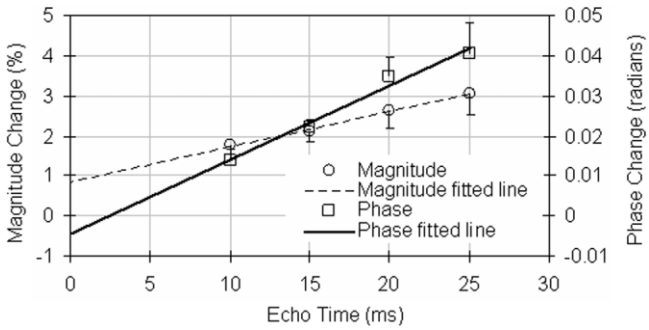


FIG. 3. TE dependence of phase and magnitude responses in a BOLD study at 9.4T. Percentage changes of magnitude (circles), and phase changes in radians (square) are linearly fitted against TEs. The average data (mean ± SEM, $N = 5$) are shown. For clarity, only one side of the error bars (SEM) is shown. The magnitude change is $\Delta S/S = 0.87 \times \text{TE(s)} + 0.0086$ ($N = 5$, $R^2 = 0.99$). The phase change is $\Delta p = 1.86 \times \text{TE(s)} - 0.0047$ ($N = 5$, $R^2 = 0.98$).

mined from the phase map with TE = 20 ms (Fig. 3). The linear fitting of magnitude changes results in a linear dependence on TE with an intercept of 0.86% ± 0.48% (mean ± SD, $N = 5$), which is significantly larger than zero ($P < 0.05$) and can be contributed to inflow effects of BOLD fMRI (32). The linear fitting of phase changes also results in a linear dependence on TE with an intercept of −0.0047 ± 0.0073 radians, which is not significantly different from zero ($P < 0.05$). The zero-intercept of phase changes indicates that inflowing arterial blood does not induce phase changes.

### Magnitude and Phase Responses in CBV-Weighted fMRI

CBV data were collected with two different TEs (interleaved in the same trial) at both 4.7T and 9.4T. Figure 4 shows the results with TE of 15 ms at 4.7T of the same animal used in Fig. 2. MRI signal decreases during stimulation as CBV increases. The dominant negative magnitude changes (violet pixels) (Fig. 4a) follow the middle of the visual cortex. A negative phase change during the activation was observed (Fig. 4b) following the middle of the cortex (violet pixels). In addition, a positive phase change (red and yellow pixels) was detected in the surrounding regions including the scalp. The magnitude and phase activation maps at the two TEs are very similar (data not shown).

In the ROI defined by the negative phase change at TE of 15 ms, the average time courses of the magnitude and phase responses were generated (Fig. 4c). In agreement with the BOLD fMRI observations, the temporal characteristics of phase and magnitude in the CBV data are extremely similar. This indicates that both magnitude and phase responses arise from the same origin: an increased CBV-induced susceptibility effect during brain activation. The spatial and temporal patterns of both magnitude and phase changes of the CBV data at 9.4T (not shown) are similar to those obtained at 4.7T (Fig. 4).

Based on the time courses, a quantitative analysis of the TE-dependent magnitude and phase changes was conducted (Fig. 5). Since the IV signal is negligible in CBV-weighted fMRI due to the short $T_2$ of arterial blood after MION injection, the intercept in the magnitude change is expected to be close to zero. At 9.4T (Fig. 5a), in the pixels with negative phase change at TE of 10 ms, both the magnitude and phase changes are linearly dependent on TE. At 4.7T (Fig. 5b), in the pixels with negative change defined by the phase activation map with TE of 15 ms, both the magnitude and phase changes are also linearly dependent on TE.

## DISCUSSION

In both the BOLD and CBV-weighted fMRI experiments, our results show similar temporal behavior for the magnitude and phase changes during activation. This indicates that the common source of magnitude and phase changes is the change of susceptibility caused by the hemodynamic response to neuronal activation. In BOLD fMRI, a positive phase change was detected in the cortical surface and midline, while a negative change was detected in the surrounding brain parenchyma and scalp (see Fig. 2b). In the CBV data, a negative change was detected in the middle cortical region, while a positive change was detected in the midline as well as the surrounding parenchyma and scalp (see Fig. 4b). Since the BOLD and CBV data differ in terms of the spatial dependence of the signal-to-noise (SNR), their phase maps may differ due to spatial variation in the

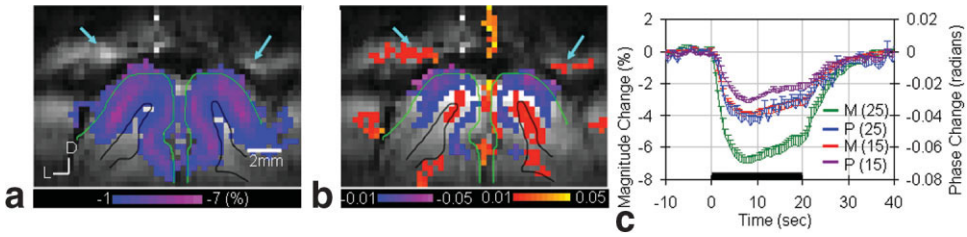


FIG. 4. Phase and magnitude responses in CBV-weighted fMRI at 4.7T. The same animal shown in Fig. 2 was used here. The relative signal change map of the magnitude (**a**) and phase-change (**b**) maps with a TE of 15 ms are overlaid on the echo-planar images. Green contours delineate the cortical surface, and black contours delineate white matter boundaries. These contours are drawn from the $T_1$-weighted anatomical image. The units of the color bars are the relative signal change for the magnitude, and the radians for the phase. L: lateral, D: dorsal. Cyan arrows point to the scalp. **c:** Averaged phase and magnitude time courses from the negative response pixels of the phase activation map (b) over five animals (mean ± SEM, $N = 5$). The unit of the $y$-axis is the percentage signal change for the magnitude, and the radians for the phase. For clarity, only one side of the error bars (SEM) is shown. M: magnitude; P: phase; the numbers in parentheses are the TE in units of milliseconds. The black rectangular bar indicates the 20-s stimulus duration.

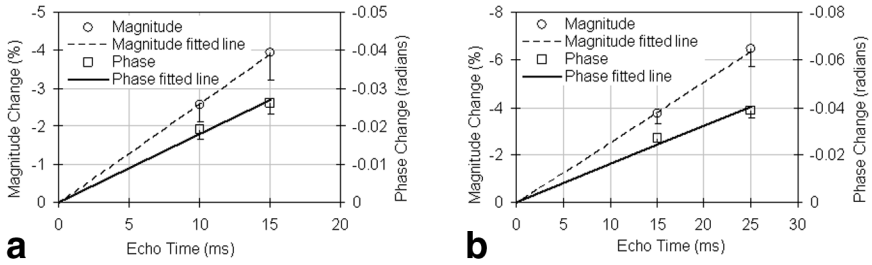


FIG. 5. TE-dependent phase and magnitude responses in CBV-weighted fMRI at 9.4T and 4.7T. Percentage changes of magnitude (circles) and phase changes in radians (square) are linearly fitted against the TEs. **a:** Average data from 9.4T (mean ± SEM, $N = 6$). **b:** Average data from 4.7T (mean ± SEM, $N = 5$). a: At 9.4T the magnitude change is $\Delta S/S = -2.60 \times$ TE(s), ($N = 6$, $R^2 = 0.996$), and the phase change is $\Delta p = -1.8 \times$ TE(s), ($N = 6$, $R^2 = 0.925$). b: At 4.7T the magnitude change is $\Delta S/S = -2.55 \times$ TE(s) ($N = 5$, $R^2 = 0.997$), and the phase change is $\Delta p = -1.6 \times$ TE(s), ($N = 5$, $R^2 = 0.868$). For clarity, only one side of the error bars is shown.

SNR. To eliminate the SNR effect, the phase maps were redisplayed with a low statistical threshold of CC = 0.1 without clustering ($P < 0.2$) in Fig. 6. Similarly to Figs. 2b and 4b, in the BOLD data a positive phase change dominates in the cortical surface and is surrounded by a negative phase change, while in the CBV data a negative phase change dominates in the middle cortical area and is surrounded by a positive phase change.

### Temperature Change as a Possible Source of the Phase Change

The local brain temperature change, which is caused by alterations in cerebral metabolic rate of oxygen consumption ($CMRO_2$) and cerebral blood flow (CBF) (33,34), can lead to a change in the brain water proton resonance frequency (13,35) and hence an fMRI phase change. Also, oxygen molecules in tissue are paramagnetic, and their density may also change during brain activation, leading to a phase change in fMRI signal. These two factors should lead to the same phase changes in both BOLD and CBV-weighted fMRI signals. This notion is inconsistent with our data, which indicates that these two factors are not the dominant source of the detected phase changes in our studies. Furthermore, the temporal characteristics of our detected phase changes are not consistent with those caused by the local temperature change detected by a thermocouple probe (33). Theoretically, during neural activation, a local increase in $CMRO_2$ generates heat, and a local elevation of CBF may supply and remove heat based on the temperature difference between incoming blood and local tissue. Hence the local temperature can increase or decrease depending on the ratio of the $CMRO_2$ change vs. the CBF change (36). Gorbach et al. (34) measured temperature in the human cerebral cortex using an infrared camera during surgery (under a large (~6°C) temperature difference between arterial blood (37°C) and the cortex (31°C)), and reported that median nerve stimulation, hand movements, finger tapping, and speech production induced temperature increases of 0.04–0.08°C in relevant areas. Using a thermocouple probe to directly measure the local temperature in the somatosensory cortex of rats, Trubel et al. (33) found an increase of ~0.08°C during two-min-long electric forepaw stimulation. Since temperature varies as a consequence of the time integral of CBF and $CMRO_2$ changes (see Eqs. [1a], [1b], and [2] in Ref. 33), the temporal change is expected to be much slower than the hemodynamic response (33). As predicted, the temperature change was found to have a time-to-peak of ~42 s and a time-to-baseline of >2 min in the rat somatosensory cortex (see Figs. 2d and 4d in Ref. 33). In the present study

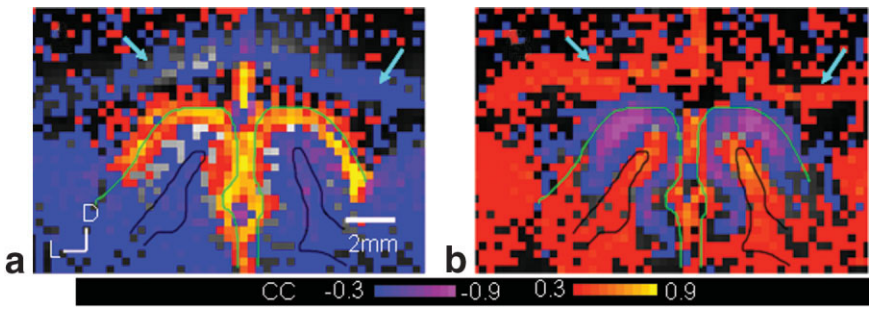


FIG. 6. Phase maps of BOLD and CBV-weighted fMRI with a low statistical threshold. Statistical CC maps with a low threshold (CC = 0.1, no clustering applied, $P \leq 0.2$) of BOLD (**a**) and CBV-weighted fMRI (**b**). The data are from the animal shown in Figs. 2 and 4. a: In the BOLD study the most significant stimulation-induced positive phase change appears in the cortical surface and is surrounded by the negative phase change. b: In the CBV-weighted fMRI study the most significant stimulation-induced negative phase change appears in the middle cortical layer and is surrounded by the positive phase change. D: dorsal, L: lateral. Cyan arrows point to the scalp. The green contours that outline the cortical surface, and the black contours that delineate the white matter were obtained from the $T_1$-weighted anatomical image and then superimposed on a and b.

the temporal characteristics of phase changes were similar to those of the magnitude changes, with the phase changes reaching their peaks within 10 s and returning to baseline in 20 s for both BOLD and CBV data (see Fig. 2c and Fig 4c). In a separate long-stimulation study (3 min) in one animal by CBV-weighted fMRI (data not shown), the temporal characteristics of phase changes remained similar to those of the data presented here, and the spatial patterns were similar to those shown in Fig. 6b. Therefore, the phase changes detected in this study were not dominated by the local temperature change.

### IV Signal as a Possible Source of the Phase Change

The IV signal (12) is also a possible source of the phase change in the fMRI signal. The MRI signal is the vector sum of the EV signal with no phase shift (see Eq. [1]) and IV signal with the phase shift induced by the blood susceptibility effect during brain activation. For CBV-weighted fMRI, since the blood $T_2$* is very short after the injection of MION (<1 ms), the IV signal is negligible at TE = 10 ms, and thus a phase change induced by IV signal cannot be detected. For BOLD fMRI, if the IV signal is the source of the phase change, the magnitude of the phase change can be estimated (12). At 9.4T the $T_2$ of venous blood is 4.9 ms at an oxygenation level of 0.6 and 6.4 ms at an oxygenation level of 0.7 (30), and blood $T_2$* is even shorter. Thus, the IV signal is 0.06–0.2% of the maximum signal intensity in a spin-echo image at a TE of 25 ms, and even less in a GE image at a TE of 25 ms. Thus, it is expected that no significant phase change can be induced by the IV signal. Our measured phase change of 0.04 radians in a GE image at a TE of 25 ms indicates that the IV signal is not the dominant source of the phase change in the BOLD data. In addition, if the IV signal is the source of the phase change, the relationship between the detected phase change and TE is not expected to be linear over a wide range of TE values (i.e., 10–25 ms) at 9.4T. A previous 7T simulation study (37) showed that the phase change increases until a maximum at TE = 12 ms, and then decreases with TE and turns negative for large TEs. The linear dependence on TE of the BOLD phase change in the range of 10–25 ms at 9.4T provides further evidence that the IV signal contribution is not the major source of the BOLD phase change.

### Physical Source of the Phase Change: Lorentz Sphere Effect

Based on the spatial and temporal characteristics of the phase changes and their TE dependence, the phase changes of BOLD and CBV-weighted fMRI can be explained by changes in volume-averaged magnetization and the demagnetization effect during activation, which is consistent with the theoretical consideration described in the Theory section. In BOLD, the deoxyhemoglobin concentration in venous blood decreases during activation, causing a decrease in the volume-averaged magnetization. Even though the exact VOA can not be obtained from 2D single-slice data, the VOA is likely to be the entire visual cortical area because all of the primary visual cortex should respond to the binocular, full-field visual stimulation used in our study. In one hemisphere, since the size of the visual cortex is larger in the posterior–anterior direction (which is roughly parallel to $\boldsymbol{B_0}$) than in the medial–lateral direction (see Fig. 2 in Ref. 38), the field change of an object with its long axis parallel to $\boldsymbol{B_0}$ is dominated by a volume-averaged magnetization change (23). The reduction in volume-averaged magnetization due to the BOLD effect decreases the magnetic field. Based on the relation between the measured phase change and the magnetic field change by the GE sequence (39), the decrease of the magnetic field leads to a positive phase change (such a relation was experimentally confirmed in our experiment; data not shown). Therefore, the decreased magnetic field of BOLD effect leads to a *positive* phase change that resides predominantly in the large draining vein area, where the venous blood volume $f$ is high. In addition to the positive phase change, a negative change due to the demagnetization effect was detected in the surrounding areas.

In CBV-weighted fMRI, the volume of high susceptibility blood increases during stimulation, which leads to an increase in the volume-averaged magnetization. Hence, the increased volume-averaged magnetization leads to a *negative* phase change primarily in the middle cortical area, where the blood volume increase, $\Delta f$, is the highest. In addition to the negative phase change, a positive phase change due to the demagnetization effect was detected in the surrounding areas. By combining the BOLD and CBV phase data, we can conclude that the measured phase change of fMRI signals is likely due to the volume-averaged magnetization change and its demagnetization effect in the Lorentz sphere model.

In the cortex, where microvessels (~10 μm in diameter) dominate (40), the local term corresponding the summation of vessels in the Lorentz sphere model can be assumed to vanish due to the random orientation of numerous vessels within the sphere. This assumption is valid in the middle cortical area. However, in the cortical surface, where larger vessels dominate, the local term does not necessarily vanish. Nonetheless, a consistent positive phase change in the cortical surface indicates that the local term is smaller than the volume-averaged magnetization and demagnetization effects. The validity of the Lorentz sphere model in the cortical surface also depends on the validity of the assumption of the continuous volume-averaged magnetization distribution within the VOA. A violation of this assumption may slightly alter the volume-averaged magnetization and demagnetization effects, but should not change the semiqualitative picture presented above.

## CONCLUSIONS

Phase changes of fMRI signal were detected in both BOLD and CBV-weighted fMRI obtained with the use of a GE-EPI sequence. The phase changes cannot be explained by the IV contribution and tissue temperature changes. The phase changes we observed during brain activation can be explained by the volume-averaged magnetization change due to the Lorentz sphere effect.

## ACKNOWLEDGMENTS

The authors thank Tsukasa Nagaoka, Noam Harel, Tiejun Zhao, and Lei Zhou for helpful discussions.

## REFERENCES


1. Ogawa S, Lee T-M, Kay AR, Tank DW. Brain magnetic resonance imaging with contrast dependent on blood oxygenation. Proc Natl Acad Sci USA 1990;87:9868–9872.
2. Ogawa S, Lee T-M, Nayak AS, Glynn P. Oxygenation-sensitive contrast in magnetic resonance image of rodent brain at high magnetic fields. Magn Reson Med 1990;14:68–78.
3. Ogawa S, Lee TM. Magnetic resonance imaging of blood vessels at high fields: in vivo and in vitro measurements and image simulation. Magn Reson Med 1990;16:9–18.
4. Kennan RP, Scanley BE, Innis RB, Gore JC. Physiological basis for BOLD MR signal changes due to neuronal stimulation: separation of blood volume and magnetic susceptibility effects. Magn Reson Med 1998;40:840–846.
5. Mandeville JB, Marota JJA, Kosofsky BE, Keltner JR, Weissleder R, Rosen BR. Dynamic functional imaging of relative cerebral blood volume during rat forepaw stimulation. Magn Reson Med 1998;39:615–624.
6. van Bruggen N, Busch E, Palmer JT, Williams S-P, de Crespigny AJ. High-resolution functional magnetic resonance imaging of the rat brain: mapping changes in cerebral blood volume using iron oxide contrast media. J Cereb Blood Flow Metab 1998;18:1178–1183.
7. Mandeville JB, Jenkins BG, Kosofsky BE, Moskowitz MA, Rosen BR, Marota JJA. Regional sensitivity and coupling of BOLD and CBV changes during stimulation of rat brain. Magn Reson Med 2001;45:443–447.
8. Ogawa S, Menon RS, Tank DW, Kim S-G, Merkle H, Ellermann JM, Ugurbil K. Functional brain mapping by blood oxygenation level-dependent contrast magnetic resonance imaging. Biophys J 1993;64:800–812.
9. Yablonskiy D, Haacke E. Theory of NMR signal behavior in magnetically inhomogeneous tissues: the static dephasing regime. Magn Reson Med 1994;32:749–763.
10. Wen H, Wolff S, Berman K, Turner R, Iadarolla M, Balaban R. Phase and magnitude functional imaging of motor tasks and pain stimuli. In: Proceedings of the 1st Annual Meeting of ISMRM, New York, NY, USA, 1993 (Abstract 9).
11. Lee AT, Glover GH, Meyer CH. Distribution of large venous vessels in time-course spiral blood-oxygen-level-dependent magnetic resonance functional neuroimaging. Magn Reson Med 1995;33:745–754.
12. Menon RS. Postacquisition suppression of large-vessel BOLD signals in high-resolution fMRI. Magn Reson Med 2002;47:1–9.
13. Yablonskiy D, Ackerman JH, Raichle ME. Coupling between changes in human brain temperature and oxidative metabolism during prolonged visual stimulation. Proc Natl Acad Sci USA 2000;97:7603–7608.
14. Woolsey TA, Rovainen CM, Cox SB, Henegar MH, Liang GE, Liu D, Moskalenko YE, Sui J, Wei L. Neuronal units linked to microvascular modules in cerebral cortex: response elements for imaging the brain. Cereb Cortex 1996;6:647–660.
15. Duong TQ, Silva AC, Lee S-P, Kim S-G. Functional MRI of calcium-dependent synaptic activity: cross correlation with CBF and BOLD measurements. Magn Reson Med 2000;43:383–392.
16. Zhao F, Wang P, Kim S-G. Cortical depth-dependent gradient-echo and spin-echo BOLD fMRI at 9.4T. Magn Reson Med 2004;51:518–524.
17. Zhao F, Wang P, Hendrich K, Uguribl K, Kim S-G. Cortical layer-dependent BOLD and CBV responses measured by spin-echo and gradient-echo fMRI: insights into hemodynamic regulation. Neuroimage 2006;30:1149–1160.
18. Peck ER. Magnetic properties of matter. Electricity and magnetism. New York: McGraw-Hill Book Company, Inc.; 1953. p 271–336.
19. Reitz JR, Milford FJ. Foundations of electromagnetic theory. New York: Addison-Wesley Publishing Company; 1967.
20. Springer CS. Physicochemical principles influencing magnetopharmaceuticals. In: Gillies R, editor. NMR in physiology and biomedicine. San Diego: Academic Press; 1994. p 75–99.
21. Durrant CJ, Hertzberg MP, Kuchel PW. Magnetic susceptibility: further insights into macroscopic and microscopic fields and the sphere of Lorentz. Concepts Magn Reson 2003;18A:72–95.
22. Ye FQ, Allen PS. Relaxation enhancement of the transverse magnetization of water protons in paramagnetic suspensions of red blood cells. Magn Reson Med 1995;34:713–720.
23. Wolber J, Cherubini A, Leach MO, Bifone A. Hyperpolarized $^{129}$Xe NMR as a probe for blood oxygenation. Magn Reson Med 2000;43:491–496.
24. Li L. Magnetic susceptibility quantification for arbitrarily shaped objects in inhomogeneous fields. Magn Reson Med 2001;46:907–916.
25. Chu SCK, Xu Y, Balschi JA, Springer CS. Bulk magnetic susceptibility shifts in NMR studies of compartmentalized samples: use of paramagnetic reagents. Magn Reson Med 1990;13:239–262.
26. Zhao F, Wang P, Harel N, Nagaoka T, Kim S-G. Contrast agent-enhanced functional magnetic resonance imaging at 4.7T and 9.4T. In: Proceedings of the 11th Annual Meeting of ISMRM, Toronto, Canada, 2003 (Abstract 1770).
27. Movshon JA, Thompson ID, Tolhurst DJ. Spatial and temporal contrast sensitivity of neurons in areas 17 and 18 of the cat's visual cortex. J Physiol 1978;283:101–120.
28. Bandettini PA, Jesmanowicz A, Wong EC, Hyde JS. Processing strategies for time-course data sets in functional MRI of human brain. Magn Reson Med 1993;30:161–173.
29. Forman SD, Cohen JD, Fitzgerald M, Eddy WF, Mintun MA, Noll DC. Improved assessment of significant activation in functional magnetic resonance imaging (fMRI): use of a cluster-size threshold. Magn Reson Med 1995;33:636–647.
30. Lee S-P, Silva AC, Ugurbil K, Kim S-G. Diffusion-weighted spin-echo fMRI at 9.4 T: microvascular/tissue contribution to BOLD signal change. Magn Reson Med 1999;42:919–928.
31. Lee AT, Glover GH, Meyer CH. Discrimination of large venous vessels in time-course spiral blood-oxygen-level-dependent magnetic-resonance functional neuroimaging. Magn Reson Med 1995;33:745–754.
32. Yacoub E, Duong TQ, Van De Moortele P, Lindquist M, Adriany G, Kim S-G, Ugurbil K, Hu X. Spin-echo fMRI in humans using high spatial resolutions and high magnetic fields. Magn Reson Med 2003;49:655–664.
33. Trubel HKF, Sacolick LI, Hyder F. Regional temperature changes in the brain during somatosensory stimulation. J Cereb Blood Flow Metab 2006;26:68–78.
34. Gorbach AM, Heiss J, Kufta C, Sato S, Fedio P, Kammerer WA, Solomon J, Oldfield EH. Intraoperative infrared functional imaging of human brain. Ann Neurol 2003;54:297–309.
35. Kuroda K, Suzuki Y, Ishihara Y, Okamoto K, Suzuki Y. Temperature mapping using water proton chemical shift obtained with 3D-MRSI: feasibility in vivo. Magn Reson Med 1996;35:20–29.
36. Collins C, Smith M, Turner R. Model of local temperature changes in brain upon fuctional activation. J Appl Physiol 2004;97:2051–2055.
37. Menon R. Simulation of BOLD phase and magnitude changes in a voxel. In: Proceedings of the 11th Annual Meeting of ISMRM, Toronto, Canada, 2003 (Abstract 1719).
38. Zhao F, Wang P, Hendrich K, Kim S-G. Spatial specificity of cerebral blood volume-weighted fMRI responses at columnar resolution. Neuroimage 2005;27:416–424.
39. Haacke EM, Brown RW, Thompson MR, Venkatesan R. Magnetic properties of tissues: theory and measurement. In: Haacke EM, Brown RW, Thompson MR, Venkatesan R, editors. Magnetic resonance imaging—physical principles and sequence design. New York: John Wiley & Sons, Inc.; 1999. p 757–762.
40. Pawlik G, Rackl A, Bing RJ. Quantitative capillary topography and blood flow in the cerebral cortex of cats: an in vivo microscopic study. Brain Res 1981;208:35–58.